Numerical Study on Liquid Droplet Internal Flow Under Shock Impact

Ben Guan,* Yao Liu,† and Chih-Yung Wen‡
Hong Kong Polytechnic University, Hung Hom, Kowloon, Hong Kong, People's Republic of China
and
Hua Shen§
King Abdullah University of Science and Technology (KAUST), Thuwal 23955-6900, Saudi Arabia

The establishment of an internal flowfield inside a single water droplet subjected to shock-wave impact is numerically and theoretically investigated. The main focus is on the description of the droplet internal flow pattern, which is believed to be one of the dominant factors in initial droplet deformation. The droplet internal flow pattern holds steady for quite a long time after the incident shock passage, and a saddle point is observed for the first time. Accordingly, the saddle point inside the droplet flow is used as a characteristic point to describe the internal flow. Cases of different incident shock strengths are tested, and a theoretical prediction is proposed to delineate the correlation between the saddle point steady position and the strength of the incident shock wave. The numerical cases are found to be in good agreement with the prediction. The present study helps to complete the understanding of the overall droplet aerobreakup phenomenon.

Nomenclature

A, B	=	constants used in the correlation
a_0	=	sound speed in air
d_0	=	initial droplet diameter
l_{sp}	=	displacement of the saddle point
l^*_{sp}	=	nondimensional displacement of the saddle point
M_s	=	incident shock Mach number
Oh	=	Ohnesorge number
Re	=	Reynolds number
t	=	dimensional time
t^*	=	nondimensional time (initiates when the incident shock impacts)
t_s	=	duration in which the shock in air influences the leeward area
t^*_{sp}	=	nondimensional time (initiates when the saddle point appears)
u_g	=	postshock airflow velocity
u_l	=	liquid flow velocity
u_s	=	shock velocity in air
u_{sp}	=	velocity of the saddle point
We	=	Weber number
x^*	=	nondimensional position at the x coordinate
γ	=	ratio of the specific heats of air
ρ_g	=	postshock air density
ρ_l	=	density of liquid
ρ_0	=	density of quiescent air

*Research Associate, Department of Mechanical Engineering, Hong Kong Special Administrative Region.

†Ph.D. Candidate, Department of Mechanical Engineering, Hong Kong Special Administrative Region.

‡Professor, Department of Mechanical Engineering, Hong Kong Special Administrative Region.

§Research Associate, Applied Mathematics and Computational Science, Computer Electrical and Mathematical Science and Engineering Division (CEMSE), Extreme Computing Research Center (ECRC).

I. Introduction

THE shock-wave-induced aerobreakup of a liquid droplet occurs in many high-speed flow scenarios and is a fundamental and challenging two-phase flow problem. Extensive studies have been conducted on this fascinating phenomenon for more than half a century because of its wide applications in chemical processing, Space Shuttle protection, high-speed vehicle propulsion, and the delivery of bulk chemical weapons. Knowledge of the deformation and fragmentation of a water droplet is of interest in establishing the mechanism of the breakup process. Comprehensive reviews of droplet breakup were written by Wierzba and Takayama [1], Guildenbecher et al. [2], Joseph et al. [3], and Theofanous [4]. However, these reviews mainly focused on the external airflow and the interface evolution induced by the shock wave because of the difficulty of visualizing the droplet internal flow.

The first experimental attempt to disclose the internal flow pattern of droplet breakup under shock impingement was conducted by Igra and Takayama [5] using a cylindrical water column. Although the qualitative breakup process and internal variation were discussed in their research, the internal flow pattern remained obscure. A recent experimental study was conducted by Sembian et al. [6], in which the internal wave system evolution and cavitation inside a cylindrical water column were visualized after the shock impact. However, the details of the internal flow and the initial deformation of the water column were still difficult to illustrate. Besides, nearly all of the studies involving droplet internal flow were conducted by numerical methods. Although several researchers [7–10] elucidated the internal flow pattern, they concentrated on cases with low Weber numbers We. In shock-induced droplet breakup cases, where the inertial effect dominates the flow, the droplet internal flowfield has been totally overlooked. The deformation of droplet configuration, however, is determined essentially by both the liquid flow inside the droplet and the external airflow. Also, in the study by Boiko and Poplavski [11], the authors inferred that the internal flow could be extremely important for constructing a unified physical model of drop breakup in a gas flow. It will be instructive to build the connections between the flow parameters and the droplet internal flow.

II. Numerical Methods

For the case of liquid droplet breakup, the dominant dimensionless parameters are the Weber number We, Ohnesorge number Oh, and Reynolds number Re. The definitions of these parameters are

$$We = \frac{\rho_g u_g^2 d_0}{\sigma}, \qquad Oh = \frac{\mu_l}{\sqrt{\rho_l \sigma d_0}}, \qquad Re = \frac{\rho_g u_g d_0}{\mu_g} \tag{1}$$

where ρ is the density; u is the velocity; d_0 is the diameter of the liquid droplet; σ is the surface tension; μ is the viscosity; and subscripts l and g represent the liquid and gas behind the shock, respectively. Weber number is the ratio of the fluid's inertial force to its surface tension force, Ohnesorge number is the ratio of the viscous force to the surface tension force, and Reynolds number is the ratio of the inertial force to the viscous force.

In the present study, in which an air shock wave impacting a single liquid droplet is simulated, Weber number and Reynolds number reached orders of $\times 10^3$ and $\times 10^4$, respectively. These results indicate that the surface tension effect and the viscosity effect are both much smaller than the inertial force. As a result, the compressible axisymmetric Euler equations are solved to simulate the shock–droplet interaction:

$$\frac{\partial \alpha}{\partial t} + V \cdot \nabla \alpha = 0 \tag{2}$$

$$\frac{\partial \rho_s \alpha_s}{\partial t} + \nabla \cdot (\rho_s \alpha_s V) = -\frac{\rho_s \alpha_s V}{y}, \qquad s = 1, 2 \tag{3}$$

$$\frac{\partial \rho V}{\partial t} + \nabla \cdot (\rho V \otimes V + p) = -\frac{\rho V \otimes V}{y} \tag{4}$$

$$\frac{\partial E}{\partial t} + \nabla \cdot (V(E + p)) = -\frac{V(E + p)}{y} \tag{5}$$

where α denotes the air volume fraction; ρ_s the density of the component fluid s; ρ the density of the mixture; V the velocity vector; p the pressure; and E the total energy.

The stiffened gas equation of state (EOS) is adopted to close this system:

$$p = (\gamma - 1)\left(E - \frac{1}{2}\rho V \cdot V\right) - \gamma\pi \tag{6}$$

where

$$\frac{1}{\gamma - 1} = \Sigma \frac{\alpha_i}{\gamma_i - 1} \quad \text{and} \quad \frac{\gamma\pi}{\gamma - 1} = \Sigma \frac{\alpha_i \gamma_i \pi_i}{\gamma_i - 1} \tag{7}$$

The total density and the sound speed of the mixture can be respectively calculated as

$$\rho = \Sigma \alpha_i \rho_i \quad \text{and} \quad c = \sqrt{\gamma(p + \pi)/\rho} \tag{8}$$

For air, the ratio of specific heat $\gamma = 1.4$ and $\pi = 0$ Pa reduce the stiffened gas EOS to the ideal gas equation. For water, empirical parameters are adopted, where $\gamma = 7.15$ and $\pi = 3.31 \times 10^8$ Pa.

The volume-fraction-based five-equation model is solved using a maximum-principle-satisfying upwind conservation element and solution element scheme. An Harten-Lax-van Leer-Contact approximate Riemann solver is employed to get the numerical fluxes between the conservation elements. The present method has shown great performance in the numerical conservative properties in both space and time, and it has proven accurate in capturing shock and simulating contact discontinuities. Numerical validation and error analysis of the present numerical methods can be found in Shen et al.'s studies [12–14].

The numerical method is first used to simulate the experiment conducted by Yi et al. [15] using a droplet diameter d_0 of 3.03 mm and an incident shock Mach number M_s of 1.39. The corresponding dimensionless numbers of their experiment were $We = 3075$, $Re = 6.41 \times 10^4$, and $Oh = 2.14 \times 10^{-3}$. A rectangular computational domain is used within which an initially quiescent water droplet with a diameter d_0 and a right-moving planar incident shock are defined. The upper boundary of the domain is defined as a symmetric axis, and the left boundary is defined as a constant inflow condition, where the postshock state is calculated by Rankine–Hugoniot relations. The outflow conditions are enforced on the lower and right boundaries by applying a zeroth-order extrapolation. To avoid the influence of the computational boundaries, a large computational domain is arranged, where the length of the domain in the x direction is 18 times the droplet radius, and the width of the domain in the y direction is six times the droplet radius. A spatially fixed Cartesian coordinate system is used in the present study, and the center of the droplet is located at (0, 0) for convenience of the initial settings. A planar incident shock is located initially at 1.2 times the droplet radius upstream of coordinates (0, 0).

The grid convergence was first tested according to the density distributions $lg(\rho)$ along the axis of symmetry, as shown in Fig. 1, where four different numbers of grids were arranged within the length of the droplet radius. The terms R140 ~ R200 denote that there were 140 ~ 200 grids arranged per droplet radius. The left inset presents a sketch of the droplet/shock-wave system after the shock-wave impact, within which RS denotes the reflected shock, IS is the incident shock, MS is the Mach stem, WS is the windward stagnation point, and LS is the leeward stagnation point. The dotted line indicates the axis of symmetry. The right inset presents an enlarged MS area (dashed square area). It can be seen that the larger the grid number is, the sharper the pressure change across the MS shock front is. The shock fronts of cases R160, R180, and R200 nearly collapse with each other, which indicates good grid convergence. Throughout this study, a mesh size of 200 grids per droplet radius was adopted.

The comparison between the numerical results and the experimental images is shown in Fig. 2, in which three distinct instants after the shock impact ($t = 0$) are selected. At $t = 40$ μs, the experimental image shows tiny corrugation (C) at the leeward surface

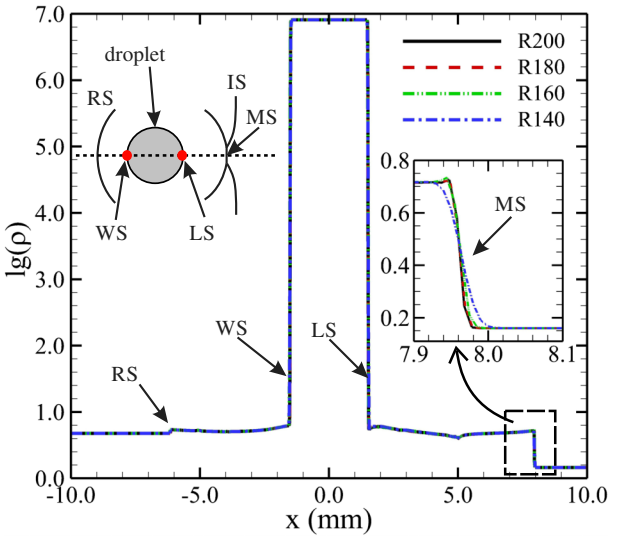

Fig. 1 Grid convergence test showing density distributions at 20 μs after the incident shock touches the droplet with four different grid sizes (140, 160, 180, and 200 grids per droplet radius).

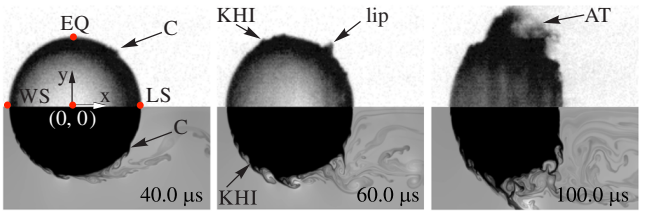

Fig. 2 Comparison of the numerical and experimental results at different instants (upper part: experimental images, lower part: numerical results).

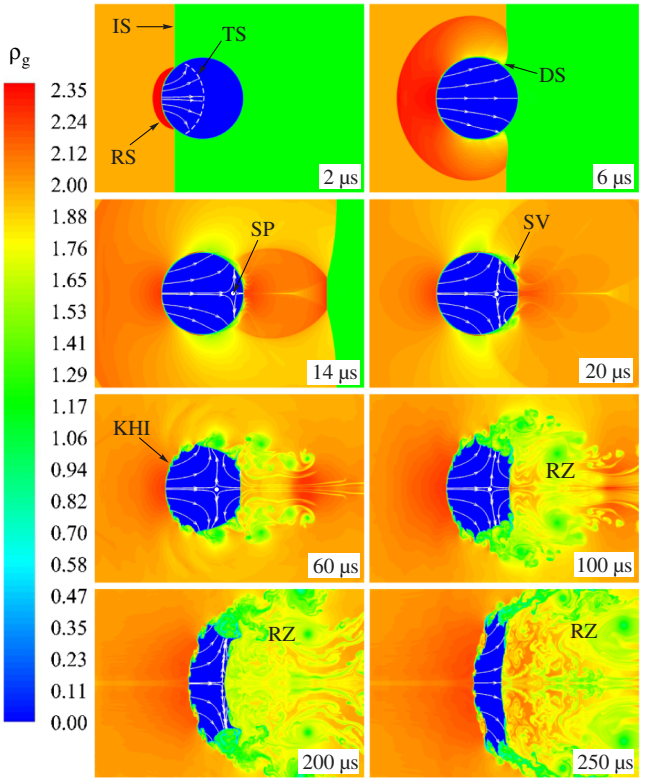

Fig. 3 Numerical airstream density distribution and the internal flow streamlines of Yi et al.'s case [15].

of the droplet between the equator (EQ) and the LS, whereas the rest of the surface remains intact. At this moment, a Kelvin–Helmholtz instability (KHI) develops at the windward surface in the numerical result but not in the experimental result. The reason for this difference derives from the neglect of the surface tension term in the present numerical method. In the experimental images, the first tiny corrugation grows at $t = 60$ μs and turns into the "lip". Also developed is the KHI amplitude. The KHI amplitude is a direct response to the shear velocity distribution, which increases from the WS to the EQ. At $t = 100$ μs, although the main body of the droplet remains spherical to a certain extent, the protrusions are distinct, and atomization (AT) occurs obviously at the tips of these protrusions. The capability of the present numerical method, according to this comparison, is proved to be fairly good.

III. Numerical Results

A. Internal Flowfield Description

The flowfield build-up process of this shock–droplet interaction is depicted in Fig. 3 by the air density contours. The white solid lines with arrows illustrate the temporal streamlines. These streamlines are truncated to focus only on the liquid flow inside the droplet rather than on the outer airflow and the interfacial boundary flow. After the IS impacts the windward surface of the droplet at $t = 2$ μs, the RS is formed and propagates upstream, whereas a transmitted shock (TS, shown by the white dash line) propagates inside the droplet, which is much faster than the incident shock in air. Before the diffracted shock (DS) collides at the droplet LS point, the droplet internal flow keeps developing induced by the internal diverging TS ($t = 6$ μs) when all of the streamlines within the droplet are pointing in the downstream direction. At $t = 14$ μs, high pressure is formed in the LS area because of the DS collision. Accordingly, the LS and the part of the internal liquid close to the LS are motivated by this high pressure to flow upstream. As a result, there must be a point inside the droplet on the axis of symmetry where the velocity is zero to balance the downstream and upstream liquid flow momentums. Observed for the first time, a saddle point (SP, labeled as the white dot) is formed. In the following instants, although the shedding vortex (SV), KHI, and

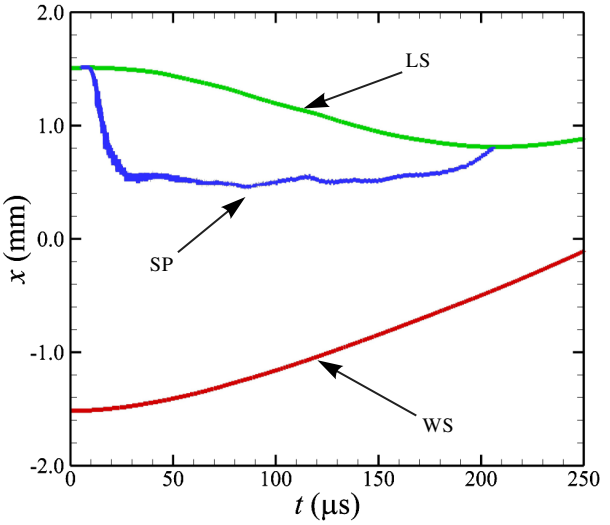

Fig. 4 Trajectories of windward stagnation point (WS), leeward stagnation point (LS), and saddle point (SP) of Yi et al.'s case [15].

chaotic recirculation zone (RZ) form in sequence ($t = 20$, 60, and 100 μs), the SP keeps its position nearly unchanged. This shock–droplet interaction process shows that the internal flowfield is established in quite a short time soon after the incident shock sweeps over the droplet. The existence of an SP suggests that the droplet is suspended in air with respect to the SP before the droplet is torn apart and blown downstream.

Late-stage images at $t = 200$ and 250 μs are shown, where the droplet is severely deformed into a crescent shape. At 200 μs, although the droplet experiences severe deformation, the internal flowfield maintains the same pattern as before. The distance between the WS and LS decreases, and the SP nearly touches the LS. At 250 μs, the SP disappears, and all of the streamlines point in the downstream direction. No longer suspended, the whole droplet drifts downstream. To delineate the relative positions of the WS, the LS, and the SP, the trajectories of these three points are recorded in Fig. 4. The distance between the WS and LS illustrates that the droplet becomes narrow in the streamwise direction. Interestingly, the SP trajectory remains steady after the internal flowfield is established (at $t = 25$ μs) and moves toward the LS when the droplet deforms severely (at $t = 180$ μs). After the trajectories of the LS and the SP intersect, the LS trajectory stops moving upstream and turns downstream instead.

More numerical cases were conducted to examine if this internal flow pattern is universal in a larger parameter space. The focus was on the droplet diameter and density differences. On the droplet diameter, additional simulations with $d_0 = 2.5$ and 3.5 mm were conducted. On the density difference, while maintaining the incident shock strength at $M_s = 2.4$, three different kinds of droplets were adopted: gelatin (heavier than water), fat (lighter that water), and dodecane (much lighter than water). The corresponding densities and stiffened gas EOS parameters are listed in Table 1.

Dimensionless trajectories of the WS, LS, and SP are extracted from the numerical results mentioned previously (see Fig. 5). The quantities are nondimensionalized as $t^* = t/[(d_0/u_g)\sqrt{\rho_l/\rho_g}]$, $x^* = x/d_0$, and $t^*_{sp} = (t - t^0_{sp})/[(d_0/u_g)\sqrt{\rho_l/\rho_g}]$, where t^* is the dimensionless time of the droplet evolution, u_g is the postshock air velocity, ρ_l is the liquid density, ρ_g is the postshock air density,

Table 1 Parameters used for the different liquids

	ρ	γ	π
Gelatin	1061.0	4.04	6.1×10^8
Fat	920.0	4.18	4.74×10^8
Dodecane	749.5	2.35	4.0×10^8

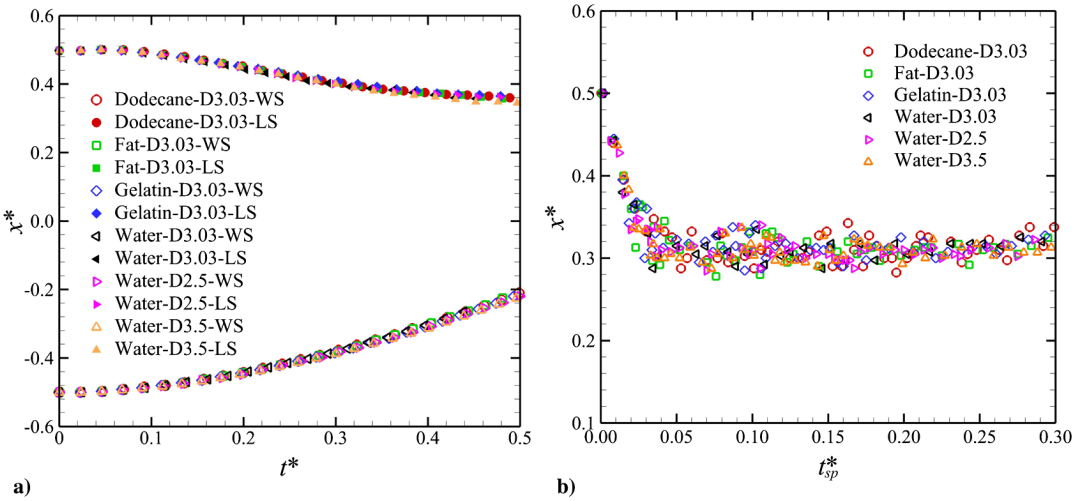

Fig. 5 Trajectories of a) WS/LS, and b) SP, for different droplets at $M_s = 2.4$ in their dimensionless form.

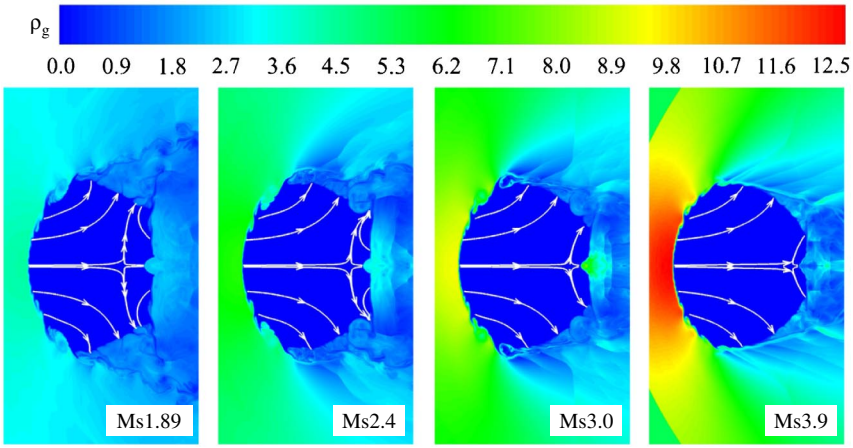

Fig. 6 Water droplet morphologies at $t^* = 0.3$ for cases with different incident shock strengths.

x^* is the dimensionless time, t^*_{sp} is the dimensionless time of SP development, and t^0_{sp} is the instant when the SP appears. It is seen from Fig. 5a that the dimensionless trajectories of the WS and LS collapse perfectly to each other. The SP trajectories, as shown in Fig. 5b, hold steady at around $x^* = 0.3$ after $t^*_{sp} = 0.05$, which indicates that this internal flow pattern is universal in similar shock/droplet interaction phenomena.

B. Internal Flowfield with Different Shock Strengths

To correlate M_s with water droplet internal flow pattern, cases with different shock strengths are simulated, and comparisons are made at the same dimensionless time. Figure 6 presents the droplet internal flow pattern at the instant when $t^* = 0.3$ for four different M_s values. It is seen that with the increase of shock strength, the SP locates itself closer and closer to the LS, and the droplet morphology varies accordingly.

The position of the SP is obviously subjected to the momentum transportation from the high-pressure zones at the WS and the LS. This momentum transportation presents itself by the movement of the positions of the stagnation points. The trajectories of the WS and LS of the preceding five different M_s cases are extracted and comparisons among them are shown in Fig. 7. It is interesting to see that both the WS and LS trajectories collapse perfectly to the potential theory prediction [16] at the early stage.

Because the internal flowfield is simple at the early stage, an easy way to describe the internal flow pattern is to record the position of the SP, which remains stationary in space after the initial flow development process. Trajectories of the SPs for different incident shock strengths are presented in Fig. 8. As shown, SPs form very

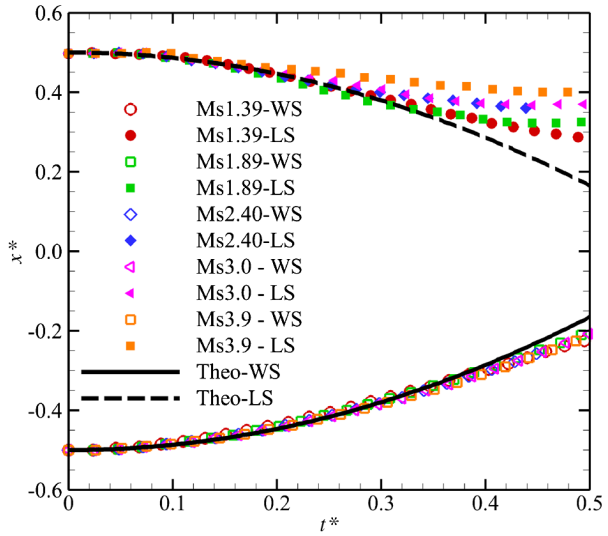

Fig. 7 Trajectories of WS (open symbols) and LS (solid symbols) of cases with different incident shock Mach numbers.

close to the LS initially and move upstream. Although oscillations exist in all five cases because of the repeated internal wave reflection, the positions of the SPs hold relatively steady after $t^*_{sp} = 0.05$. Furthermore, the trend shown in Fig. 6 is well reflected in Fig. 8 in that the SP position drifts farther downstream (larger x coordinate) for the relatively strong shock cases. The trajectories of the SPs before

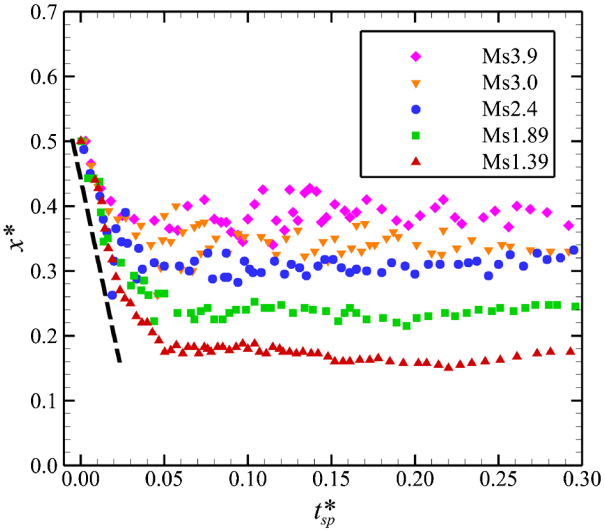

Fig. 8 SP trajectories for cases with different incident shock strengths.

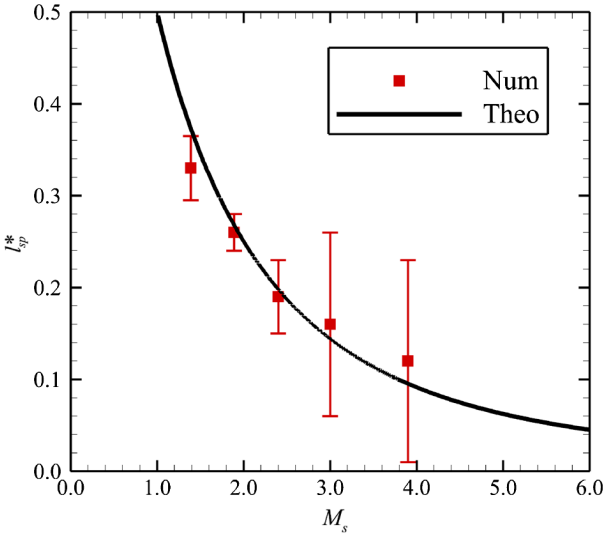

Fig. 9 Comparison of numerical results and the theoretical prediction of Eq. (10).

they reach their stationary position collapse to the same line (with the same slope as the black dash line denoted in Fig. 8). This indicates that the rate of change of the internal flow pattern can be well correlated using the preceding nondimensionalization method.

C. Theoretical Prediction

Following the preceding discussion, the displacement of the SP, $l_{\rm sp}$, after the initial shock–droplet interaction, can be estimated based on the velocity at which the SP moves ($u_{\rm sp}$) and the duration in which the shock influences the LS area (t_s), i.e., $l_{\rm sp} \sim u_{\rm sp} t_s$. $u_{\rm sp}$ is the outcome of the change of internal flow, and it can be connected to the liquid flow velocity u_l (i.e., $u_{\rm sp} \sim u_l$). The term t_s is closely related to the shock propagation outside of the droplet, and it can be connected to the shock velocity u_s by $t_s \sim (d_0/u_s) = (d_0/a_0 M_s)$, where a_0 is the sound speed in quiescent air. In this way, we present the dimensionless SP displacement $l^*_{\rm sp} = l_{\rm sp}/d_0$ by a simple linear approximation:

$$l^*_{\rm sp} = A\frac{u_l t_s}{d_0} + B = A\frac{t_s}{d_0/u_l} + B = A\frac{t_s}{\tilde{t}} + B \tag{9}$$

where d_0 on the right-hand side of the first equals sign is used to nondimensionalize the term $u_l t_s$. The liquid flow velocity is obtained qualitatively by $u_l \sim u_g\sqrt{\rho_g/\rho_l}$ as applied by Nicholls and Ranger [17], which arises directly from an application of Newton's second law to droplet displacement. The important measure of the intensity of the interaction is given by the gas-flow dynamic pressure ($(1/2)\rho_g u_g^2$ behind the shock); the momentum flux change $\rho_l u_l^2$ inside the droplet is proportional to $(1/2)\rho_g u_g^2$ as a prompt consequence of the interfacial response to this gasdynamic impulse (i.e., $\rho_l u_l^2 \sim (1/2)\rho_g u_g^2$). Therefore, the liquid velocity $u_l \sim u_g\sqrt{\rho_g/\rho_l}$ can be qualitatively obtained. The term $\tilde{t} = d_0/u_l$ can be considered as a characteristic time. A and B are constants to be determined.

Manipulating Eq. (9) and correlating the dimensionless SP displacement to the incident shock strength, we have

$$\begin{aligned} l^*_{\rm sp} &= \frac{A}{d_0} u_g \sqrt{\frac{\rho_g}{\rho_l}}\frac{d_0}{u_s} + B \\ &= A\sqrt{\frac{\rho_0}{\rho_l}}\frac{2(M_s^2-1)}{M_s\sqrt{M_s^2(\gamma^2-1)+2(\gamma+1)}} + B \end{aligned} \tag{10}$$

where ρ_0 is the density in quiescent air, and $\gamma = 1.4$ is the ratio of the specific heats of air. Note that

$$\rho_g = \rho_0\frac{(\gamma+1)M_s^2}{(\gamma-1)M_s^2+2} \tag{11}$$

$$u_g = \left(1-\frac{\rho_0}{\rho_g}\right)u_s \tag{12}$$

Asymptotic conditions are employed to confine the correlation between $l^*_{\rm sp}$ and M_s in Eq. (10). When M_s approaches 1, the incident shock is infinitely weak, and the SP is located at the center of the droplet (i.e., $l^*_{\rm sp}$ goes to 0.5). However, when M_s approaches infinity, the SP reaches the LS (i.e., $l^*_{\rm sp}$ goes to zero). From this, constants $A = -7.14$ and $B = 0.5$ are derived. Equation (10) relates the stationary SP position solely to the incident shock strength M_s.

Following the preceding discussion, the relationship between $l^*_{\rm sp}$ and M_s in Eq. (10) is depicted in Fig. 9, together with the numerical data in Fig. 8. It is seen that the theoretical prediction agrees well with the numerical simulations. The characteristic internal flowfield pattern with different incident shock strengths can be quantitatively predicted, including the stationary SP position and the trajectories of the WS and LS.

IV. Conclusions

In summary, the internal flow pattern of a single water droplet under shock impact is investigated numerically and theoretically. Similar internal flow patterns are found in cases with different incident shock strengths, in which the SP forms and remains stationary soon after the passage of the incident shock. With the increase in the incident shock strength, the SP position varies, and the droplet presents different morphologies. A simple theory is proposed to predict the stationary position of SP in accordance with the incident shock Mach number. This correlation connects the shock strength with the droplet internal flowfield. It infers that the droplet internal flow pattern is input into the droplet at the initial impact stage by the shock rather than following the postshock airstream. Upon this point, more research should be done in the near future.

Acknowledgments

This research was supported by projects of the Research Grants Council of Hong Kong, under contracts CRF C5010-14E and GRF 152151/16E, and of the Natural Science Foundation of China, number 11372265. The authors are very grateful to anonymous referees for the time spent reading and analyzing the manuscript. The many insightful remarks helped the authors improve the quality of the paper.

References

[1] Wierzba, A., and Takayama, K., "Experimental Investigation of the Aerodynamic Breakup of Liquid Drops," *AIAA Journal*, Vol. 26, No. 11, 1988, pp. 1329–1335. doi:10.2514/3.10044

[2] Guildenbecher, D., López-Rivera, C., and Sojka, P., "Secondary Atomization," *Experiments in Fluids*, Vol. 46, No. 3, 2009, pp. 371–402. doi:10.1007/s00348-008-0593-2

[3] Joseph, D. D., Belanger, J., and Beavers, G., "Breakup of a Liquid Drop Suddenly Exposed to a High-Speed Airstream," *International Journal of Multiphase Flow*, Vol. 25, No. 6, 1999, pp. 1263–1303. doi:10.1016/S0301-9322(99)00043-9

[4] Theofanous, T., "Aerobreakup of Newtonian and Viscoelastic Liquids," *Annual Review of Fluid Mechanics*, Vol. 43, 2011, pp. 661–690. doi:10.1146/annurev-fluid-122109-160638

[5] Igra, D., and Takayama, K., "Investigation of Aerodynamic Breakup of a Cylindrical Water Droplet," *Atomization and Sprays*, Vol. 11, No. 2, 2001, p. 20.

[6] Sembian, S., Liverts, M., Tillmark, N., and Apazidis, N., "Plane Shock Wave Interaction with a Cylindrical Water Column," *Physics of Fluids*, Vol. 28, No. 5, 2016, Paper 056102.

[7] Wadhwa, A. R., Magi, V., and Abraham, J., "Transient Deformation and Drag of Decelerating Drops in Axisymmetric Flows," *Physics of Fluids*, Vol. 19, No. 11, 2007, Paper 113301. doi:10.1063/1.2800038

[8] Theofanous, T., Mitkin, V., and Ng, C., "The Physics of Aerobreakup. 3. Viscoelastic Liquids," *Physics of Fluids*, Vol. 25, No. 3, 2013, Paper 032101. doi:10.1063/1.4792712

[9] Qu, Q., Ma, P., Liu, P., Li, S., and Agarwal, R. K., "Numerical Study of Transient Deformation and Drag Characteristics of a Decelerating Droplet," *AIAA Journal*, Vol. 54, No. 2, 2016, pp. 490–505.

[10] Shao, C., Luo, K., and Fan, J., "Detailed Numerical Simulation of Unsteady Drag Coefficient of Deformable Droplet," *Chemical Engineering Journal*, Vol. 308, Jan. 2017, pp. 619–631. doi:10.1016/j.cej.2016.09.062

[11] Boiko, V., and Poplavski, S., "On the Dynamics of Drop Acceleration at the Early Stage of Velocity Relaxation in a Shock Wave," *Combustion, Explosion, and Shock Waves*, Vol. 45, No. 2, 2009, pp. 198–204. doi:10.1007/s10573-009-0026-4

[12] Shen, H., Wen, C.-Y., and Zhang, D.-L., "A Characteristic Space–Time Conservation Element and Solution Element Method for Conservation Laws," *Journal of Computational Physics*, Vol. 288, May 2015, pp. 101–118. doi:10.1016/j.jcp.2015.02.018

[13] Shen, H., and Wen, C.-Y., "A Characteristic Space–Time Conservation Element and Solution Element Method for Conservation Laws 2. Multidimensional Extension," *Journal of Computational Physics*, Vol. 305, Jan. 2016, pp. 775–792. doi:10.1016/j.jcp.2015.11.017

[14] Shen, H., Wen, C.-Y., Parsani, M., and Shu, C.-W., "Maximum-Principle-Satisfying Space-Time Conservation Element and Solution Element Scheme Applied to Compressible Multifluids," *Journal of Computational Physics*, Vol. 330, Feb. 2017, pp. 668–692. doi:10.1016/j.jcp.2016.10.036

[15] Yi, X., Zhu, Y., and Yang, J., "On the Early-Stage Deformation of Liquid Drop in Shock-Induced Flow," edited by G. Ben-Dor, O. Sadot, and O. Igra, *Proceedings of the 30th International Symposium on Shock Waves*, Vol. 2, Springer, Cham, Switzerland, 2017.

[16] Engel, O. G., "Fragmentation of Waterdrops in the Zone Behind an Air Shock," *Journal of Research of the National Bureau of Standards*, Vol. 60, No. 3, 1958, pp. 245–280. doi:10.6028/jres.060.029

[17] Nicholls, J., and Ranger, A., "Aerodynamic Shattering of Liquid Drops," *AIAA Journal*, Vol. 7, No. 2, 1969, pp. 285–290. doi:10.2514/3.5087